九州大学学術情報リポジトリ
Kyushu University Institutional Repository

Thermal conductivity measurement of an individual millimeter-long expanded graphite ribbon using a variable-length T-type method

Wu, Si
Research Center of Solar Power & Refrigeration, School of Mechanical Engineering, Shanghai Jiao Tong University

Li, Qin-Yi
Department of Aeronautics and Astronautics, Kyushu University

Ikuta, Tatsuya
Department of Aeronautics and Astronautics, Kyushu University

Morishita, Kazuhiko
Department of Aeronautics and Astronautics, Kyushu University

他

https://hdl.handle.net/2324/4363564

出版情報：International Communications in Heat and Mass Transfer. 171 (121115), 2021-06-01. Elsevier
バージョン：
権利関係：

KYUSHU UNIVERSITY

Thermal conductivity measurement of an individual millimeter-long expanded graphite ribbon using a variable-length T-type method

Si Wu [a], Qin-Yi Li [b, c, *], Tatsuya Ikuta [b, c], Kazuhiko Morishita [b], Koji Takahashi [b, c], Ruzhu Wang [a], Tingxian Li [a, **]

[a] Research Center of Solar Power & Refrigeration, School of Mechanical Engineering, Shanghai Jiao Tong University, Shanghai, 200240, PR China

[b] Department of Aeronautics and Astronautics, Kyushu University, Fukuoka, 819-0395, Japan

[c] International Institute for Carbon-Neutral Energy Research (WPI-I^{2}CNER), Kyushu University, Fukuoka, 819-0395, Japan

Cite this: Si Wu, Qin-Yi Li, Tatsuya Ikuta, Kazuhiko Morishita, Koji Takahashi, Ruzhu Wang, Tingxian Li. Thermal conductivity measurement of an individual millimeter-long expanded graphite ribbon using a variable-length T-type method. International Journal of Heat and Mass Transfer, 171, 121115, 2021. https://doi.org/10.1016/j.ijheatmasstransfer.2021.121115

Abstract

Expanded graphite (EG) is a well-known carbon derivative and widely used as the thermally conductive enhancer for thermal management composites. However, the accurate thermal conductivity measurement of an individual EG particle is still unexploited, which prevents the exploration of the coupling mechanism between EG and matrices and further measures for thermal conductivity enhancement. Herein, using a variable-length T-type method, we measure the thermal conductivity of an individual expanded graphite ribbon (EGR) obtained by mechanically compressing a separate EG particle. The EGR has a micrometer-sized thickness and a millimeter-sized length. By changing the sample length while maintaining the contact junction, we simultaneously obtained the thermal conductivity of the EGR and the thermal contact resistance between the sample and the probe. The longitudinal thermal conductivity of the EGR reaches up to 335.6±27.4 W m^{-1} K^{-1} at room temperature and decreases to 254.8±20.8 W m^{-1} K^{-1} as the temperature rises from 300 K to 380 K. With a higher thermal conductivity than most graphene paper products and some carbon fibers, this low-cost

*Corresponding author.
**Corresponding author.
E-mail address: qinyi.li@aero.kyushu-u.ac.jp (Qin-Yi Li), Litx@sjtu.edu.cn (Tingxian Li).

nanocarbon-based material exhibits a great advantage in the development of thermally conductive composites, and the presented accurate thermal conductivity provides indispensable data for the rational design of composites.

Keywords: Expanded graphite; graphite ribbon; variable-length T-type method; thermal conductivity; thermal contact resistance

1. Introduction

Thermal management technology based on advanced functional materials has drawn wide attention toward the temperature regulation of electronics and thermal energy storage [1]. For these applications, superior thermal transport is always desired to fast spread or extract heat, which requires substantial improvement in thermal conductivity of functional materials. Owing to their intrinsic high thermal conductivity, graphite and its derivatives including expanded graphite, carbon nanotube, graphite nanoplatelet, and graphene nanosheet have been widely used as the building block to construct bulk heat conductor or as the thermally conductive additives to improve the thermal conductivity of organics like macromolecular polymer or micromolecular phase change materials [2-4]. To better understand the coupling mechanism among different materials and boost the thermal conductivity of bulk materials, characterizations of the thermal conductivity of the individual small-sized graphite derivative is of vital importance [5].

Among various graphite derivatives, expanded graphite or exfoliated graphite (EG) is a well-known material produced from graphite intercalation compounds and featured by a high separation degree of a substantial portion of the carbon layers in the graphite [6,7]. The exfoliation process resulting in this separation can involve chemical, mechanical, and thermal methods, and the separation occurs between adjacent carbon layers, but typically not all the carbon layers are separated. Compared to the single carbon layer of graphene, EG can be considered as the intermediate product in the synthesis procedure of graphene nanosheet from graphite and shows the porous structure and high specific surface area [8]. Because of the low cost and easy synthesis of EG, the past decades have witnessed a rapid growth of research efforts on the role of EG in enhancing the thermal property of organics [9-12]. Fig. 1 shows the statistics of

open publications related to EG. It can be seen that the research topic on the thermal property of materials related to EG has been rapidly increasing for the past twenty years.

In practical applications, EG is always in the form of either its original state or the compressed state. Many investigations have employed EG particles as the porous matrix to prepare bulk compressed EG block or as the supporting material to absorb the liquid organics and then be compressed into composite block [13-16]. In these cases, the individual EG particle would become a compressed ribbon-like graphite sheet in the resulting bulk material, which can be considered as the expanded graphite ribbon (EGR). Therefore, it is very necessary to characterize the thermal conductivity of an individual EGR. To our best knowledge, there have not been reports about the investigation of the thermal conductivity of an individual EGR untill now. Unlike the graphene nanosheet and carbon nanotube [17-20], EG is generally in an irregular shape, which makes it difficult to characterize its thermal conductivity. Typically, an individual EG particle obtained by thermal exfoliation shows a worm-like or fiber-like cylinder in the submillimeter scale [7].

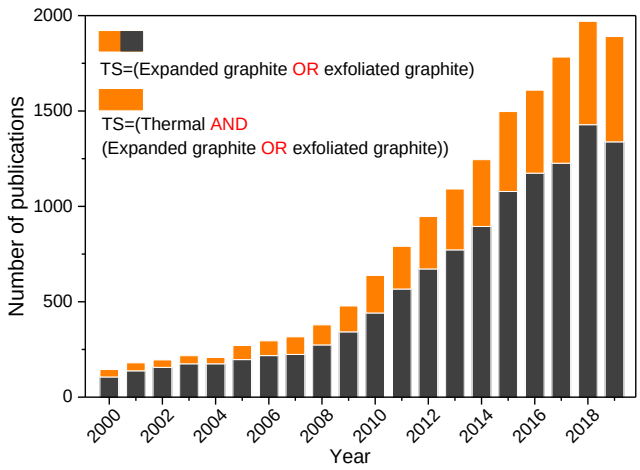

Fig. 1. The statistic of publications related to expanded graphite or exfoliated graphite (EG) and thermal conductivity. The data is retrieved from Web of Science (by 10/09/2020) and TS presents the theme subject.

Challenges are still existing in thermal measurements of small-sized or

micro/nanoscale materials, even no widely accepted standards. Several kinds of experimental techniques have been developed to measure the thermophysical properties of the small-sized fiber-like and ribbon-like materials, including the steady-state method, 3ω method [21,22], laser flash method [23], the Angstrom method [24], thermoreflectance microscopy [25], and others like Raman spectroscopy and micro-electromechanical system method (MEM) for micro/nanoscale materials [26-30]. Among these techniques, the contact method is commonly used to directly measure the thermal conductivity of an individual fiber, but the thermal contact resistance (TCR) between the fiber, thermocouple, and substrate is generally not adequately considered. As a steady-state and contact method, the T-type probe method, first developed by Zhang *et al.* [31], is especially suitable to measure the thermal conductivity of individual fiber- or ribbon-like materials [31-42]. However, the accurate thermophysical property measurement of individual micro/nanoscale materials has never been an easy task. One of the great challenges is how to determine the thermal contact resistance (TCR) between the sample and the temperature sensor [38, 42], which can sometimes cause large uncertainties to the thermal conductivity measurement. Li and co-workers [23,41,42] developed several Raman mapping techniques to determine the TCR between 1D materials. Wang *et al.* [35,38] modified the T-type probe method by adopting a variable-length technique to simultaneously measure the TCR and the thermal conductivity of a single carbon fiber.

In this work, we present the thermal conductivity measurement of an individual expanded graphite ribbon (EGR) using the variable-length T-type method developed by Wang *et al.* [35,38]. In this method, the sample length is changed several times while maintaining the contact junction between the sample and probe to simultaneously obtain the thermal resistance of the sample itself and TCR. The thermal conductivity of the EGR reaches up to 335.6 ± 27.4 W m^{-1} K^{-1} at room temperature and decreases with increasing temperature.

2. Materials and method

2.1. Materials

The expanded graphite (EG) was generated from the graphite intercalation compounds (mesh 30, type KP-100, purchased from Shanghai Yi Fan Graphite Co. Ltd., China) by thermal exfoliation following the method introduced in Ref. [20]. The EGR was obtained by mechanically compressing the EG particle (perpendicular to the axis of EG particle). The maximum pressure was 20 MPa.

2.2. Characterizations

The microstructures of the samples were characterized using a Field-emission Scanning Electron Microscopy (FE-SEM, Sirion 200 instrument, FEI Company, USA). X-ray photoelectron spectroscopy (XPS) measurement was performed on a Model K-Alpha instrument (ThermoFisher Scientific Company, US) using a monochromated Al Kα source and a pass energy of 50 eV at a base pressure of 1×10^{-8} mbar. X-ray Diffractometer (XRD) pattern was measured with a Poly-functional X-ray diffractometer (3 kW/*D8 ADVANCE Da Vinci, Germany) with Cu Kα radiation. N_2 sorption isotherm curves were measured using Gas Sorption Analyzer (24/Autosorb-IQ3, China).

2.3. Variable-length T-type method

In this method, a hot wire serves simultaneously as a heater with homogeneous heat generation and as a thermometer [31]. Generally, the platinum (Pt) wire is used as the hot wire due to its good temperature-dependent resistance. As illustrated in Fig. 2a, three heat sinks are fixed on a ceramic substrate, two of which support a thin Pt wire and maintain its initial temperature at both ends. One end of the fiber-like sample is fixed on the rest heat sink and the other on the middle position of Pt wire by conductive silver colloid. During the measurement, the whole test module is put in a chamber with high vacuum lower than 3×10^{-4} Pa and controlled temperature. Before attaching the sample to the Pt wire, the thermal and electrical properties of the bare Pt wire are first calibrated to obtain the temperature-resistance coefficient and radiation heat transfer coefficient by applying a direct current to the bare Pt wire. The temperature distribution along the Pt wire would change due to the joule heating and alter to a stable state like the parabolic shape as shown in Fig. 2b. The convection heat loss can be ignored because the whole test module is installed in a vacuum chamber. Whereas the radiation

heat loss has a strong effect on the measurement results. Considering the radiation heat loss and conduction heat loss from the Pt wire, the average temperature rise of the hot wire, ΔT, varies linearly with the heating power, UI, (U and I are the voltage and current on the Pt wire, respectively), and the slope, k_h, is obtained by [35]:

$$k_h = \frac{1}{C_h}\left\{\frac{1}{b_h}\left[\frac{1}{\sinh(2b_h)} - \frac{1}{\tanh(2b_h)}\right] + 1\right\} \tag{1}$$

where $C_h = l_h \pi D_h h$, $b_h = (h/D_h/\lambda_h)^{1/2} l_h$. λ_h, l_h, and D_h are the thermal conductivity, length, and diameter of the Pt wire, respectively. h is the heat transfer coefficient, calculated by $h \approx 4\varepsilon\sigma T_0^3$, with the surface emissivity ε and Stefan–Boltzmann constant σ (=5.67×10^{-8} W m^{-2} K^4). Since the current (I) and voltage (U) are measured by digital multimeters, ΔT can be calculated from the change of electrical resistance during the Joule heating:

$$\Delta T = \frac{\Delta Re}{\beta Re_o} \tag{2}$$

where Re_0 is the electrical resistance of the hot wire at 0 °C, β is the temperature coefficient of the resistance, and ΔRe is the electrical resistance change from that at the initial temperature. With the thermal conductivity of Pt thermometer (λ_h) [45], the heat transfer coefficient of the Pt wire, h, can be determined using Equation (1).

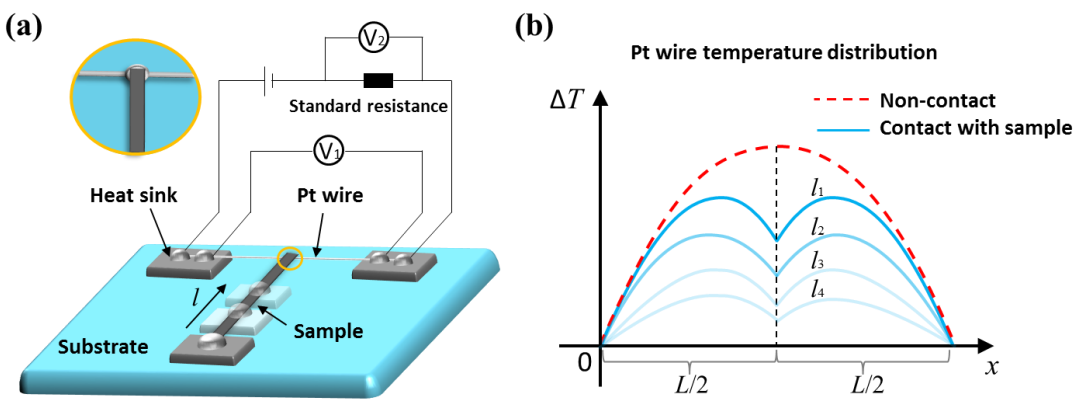

Fig. 2. Schematic diagram of variable-length T-type method. (a) The configuration of the test module. (b) Temperature distribution along the hot Pt wire before and after contacting the sample with length decreasing from l_1 to l_4. L represents the length of the Pt wire.

After the one end of the test sample is attached to the center of the Pt wire and the other end to the third heat sink, some of the Joule heating from the Pt wire leaks out through the sample. Since the width of the sample is far smaller than the length of the Pt wire, the thermal transport in the thin ribbon-like sample can be considered as one dimension, and the temperature profile along the wire is changed from the parabolic shape into the saddle shape (Fig. 2b). The solution to the one-dimensional steady-state heat conduction equation for the Pt wire and the sample gives the slope of the average temperature rise of the Pt wire with the attached sample versus the heating power:

$$k_{\Delta T\text{-}UI} = \frac{1}{C_{\mathrm{h}}}\left\{\begin{array}{l} 1+\dfrac{1}{b_{\mathrm{h}}}(e^{-b_{\mathrm{h}}}-1)+\dfrac{1}{b_{\mathrm{h}}}[1-\cosh(b_{\mathrm{h}})] \\ \times\dfrac{4b_{\mathrm{h}}\chi(l_{\mathrm{s}})e^{-b_{\mathrm{h}}}+(1-e^{-b_{\mathrm{h}}})R_{\mathrm{h}}}{\sinh(b_{\mathrm{h}})R_{\mathrm{h}}+4b_{\mathrm{h}}\chi(l_{\mathrm{s}})\cosh(b_{\mathrm{h}})} \end{array}\right\} \tag{3}$$

where R_{h} is the thermal resistance of the Pt hot wire and $\chi(l_{\mathrm{s}})$ is the apparent thermal resistance of the sample. They can be expressed by:

$$R_{\mathrm{h}} = \frac{l_{\mathrm{h}}}{\lambda_{\mathrm{h}} S_{\mathrm{h}}} \tag{4}$$

$$\chi(l_{\mathrm{s}}) = R_{\mathrm{r}} + \frac{\tanh(2b_{\mathrm{s}})}{2b_{\mathrm{s}}} R_{\mathrm{s}} + R_{c} \tag{5}$$

where, $b_{\mathrm{s}} = (h_{\mathrm{s}}/D_{\mathrm{s}}/\lambda_{\mathrm{s}})^{1/2} l_{\mathrm{s}}$, h_s is the heat transfer coefficient of the sample, calculated by $h_{\mathrm{s}} \approx 4\varepsilon_{\mathrm{s}}\,\sigma T_0^3$, D_{s} is the equivalent diameter of the EGR, $D_{\mathrm{s}}=P_{\mathrm{s}}/S_{\mathrm{s}}$ (P_{s} and S_{s} are the perimeter and area of the section of the EGR, respectively), l_{s} is the effective length of the EGR, S_{h} is the cross-sectional area of the Pt wire, R_{r} is the TCR between the sample and the heat sink, R_{c} is the TCR between the sample and the hot wire, and R_{s} is the thermal resistance of the sample defined by:

$$R_{\mathrm{s}} = \frac{l_{\mathrm{s}}}{\lambda_{\mathrm{s}} S_{\mathrm{s}}} \tag{6}$$

The subscript s mentioned above denotes the tested sample.

From Equation (3), the apparent thermal resistance of the sample, $\chi(l_{\mathrm{s}})$, is

calculated from:

$$\chi(l_s) = \frac{R_h}{4b_h} \frac{2[1-\cosh(b_h)] - b_h \sinh(b_h)(k_{\Delta T\text{-}UI} C_h - 1)}{\sinh(b_h) + b_h \cosh(b_h)(k_{\Delta T\text{-}UI} C_h - 1)} \tag{7}$$

Here, the basic concept of the present variable-length T-type probe method is illustrated in Fig. 2a, which shows that the contact junction between the tested sample and Pt hot wire keeps unchanged as the effective length of the sample is shortened. According to Madhusudana's analysis of the solid spot TCR of a joint, R_r can be neglected compared to R_c because the actual contact area between the sample and the heat sink is much larger than that at the junction between the sample and the Pt hot wire [35]. Thus, Equation (5) can be simplified to:

$$\chi(l_s) \approx \frac{\tanh(2b_s)}{2b_s} R_s + R_c \tag{8}$$

When the effective length of the sample is shortened by moving the third heat sink toward the Pt wire, the changes in the average temperature rise of the Pt hot wire can be solely determined because R_c is constant. Fig. 2b shows the change tendency in the temperature rise of the hot wire for different sample lengths (l_s). If the sample is shortened from l_1 to l_2 with keeping the contact condition between the sample and the hot wire unchanged, two apparent thermal resistances $\chi(l_1)$ and $\chi(l_2)$ can be obtained according to Equation (7). Assuming that radiation heat loss from the test sample is known, two unknown parameters, i.e. the thermal conductivity of sample (λ_s) and the TCR at the junction (R_c) can be simultaneously obtained by fitting the apparent thermal resistance at two different lengths using Equations (6) and (8). In this work, four different sample lengths were used to extract the thermal conductivity of test samples so as to improve measurement accuracy.

2.4. Test system and procedures

The sample holder is made of three silicon wafers and mounted on a homemade ceramic substrate. The Pt wire with a purity of over 99.98% is used as the hot wire about 30 μm in diameter and 8 mm in length. The temperature-resistance coefficient of Pt at room temperature is 0.00392 K^{-1} [35]. Compared to the Pt wire and the sample, the silicon wafer has a much larger heat capacity and smaller thermal resistance so that

they can act as heat sinks with a constant temperature. The conductive silver colloid is used to connect both ends of Pt wire with the silicon wafer. Then, the ceramic substrate is loaded into the vacuum chamber (Oxford Instruments, Optistat DN-V), which is continuously evacuated by a vacuum pump (R5614Y-Z, 1400 rpm) and a turbomolecular pump (Leybold TW70H, 72 000 rpm). The chamber is held at room temperature while a power supply (Advantest R6243) is used to supply various currents to the hot wire. The electrical resistance of the hot wire is measured using the four-probe technique with two digital multimeters (Keithley 2002, 8.5 digits) and a standard resistor (Yokogawa 2792, 1). All the measurements were carried out in a vacuum of about 1×10^{-4} Pa so that the heat convection loss from the Pt wire and sample could be neglected. Fig. 3 shows the schematic of the experimental apparatus and the circuit for measuring the electrical resistance of the hot wire. The photoes of the main part of test system is demonstrated in Fig. S1.

After measuring the temperature-resistance coefficient and radiation heat transfer coefficient of the bare Pt wire, one end of a long and straight sample (EGR) with a width of about 400 μm is attached to the middle position of Pt wire and the other to the silicon wafer by using the silver glue as the adhesion material to minimize the junction resistance. Then, the substrate is loaded into the vacuum chamber again to measure the electrical resistance change of the hot wire with the attached sample. After one group measurement is completed, one silicon wafer attached with one end of the sample is moved toward the Pt wire to shorten the effective length of the sample. This operation is performed by dissolving the silver glue using an organic solvent to separate the end of the sample from the silicon wafer and then attaching it to the silicon wafer again in the next length. After using the silver glue to attaching the sample every time, the substrate is put into a vaccuum oven for heat treatment at 180 ^{o}C overnight to ensure the stable junction contact. Because the sample is contacted with the silicon wafer and covered by silver glue, it can be thought that the invalid part of the sample length will not affect the result. In this way, the effective sample length is decreased while maintaining the contact junction between the sample and the hot wire. This operation is repeated for all the sample lengths.

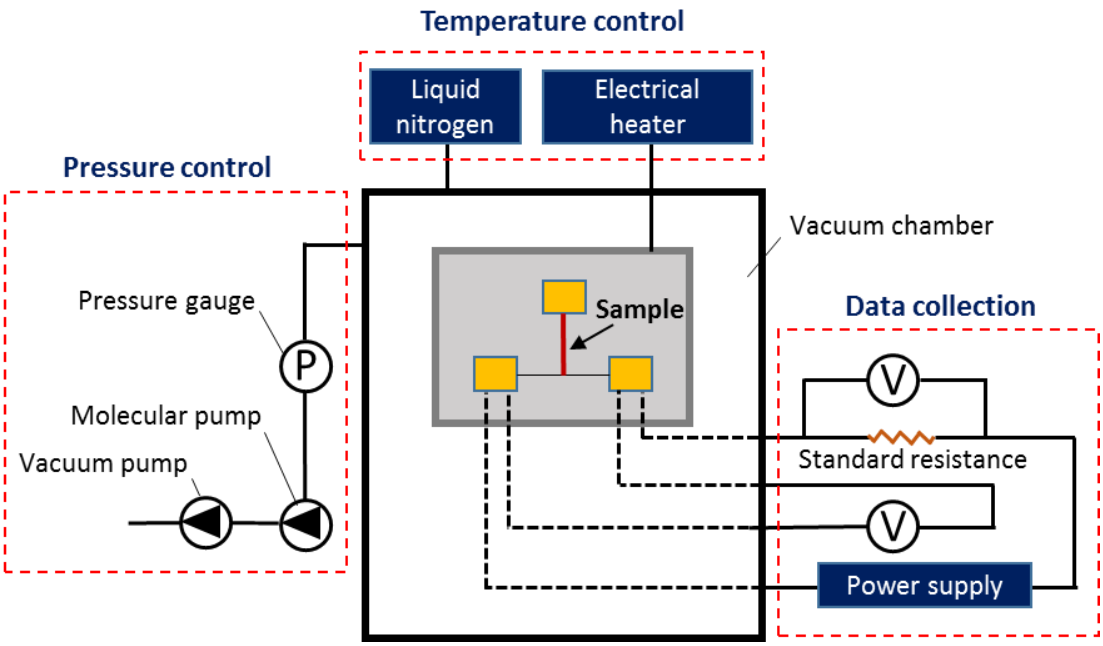

Fig. 3. Schematic of the experimental apparatus and measurement system.

3. Results and discussion

3.1. Morphology and structural characterization

The microstructure evolution from the graphite intercalation compounds (GICs) to the EGR is firstly investigated and demonstrated as illustrated in Fig. 4. As the parent material of EG and EGR, the GICs composed of a great number of van-der-Waals-bonded graphite nanoplatelets (GNPs) are obtained by chemical intercalation treatment of the raw graphite flake and show the compact lamellar structure with interlayer space in submicron width (Fig. 4a). After the thermal exfoliation treatment, the interlayer space is largely extended to several microns to obtain the loose, porous, and worm-like EG (Fig. 4b). That is due to the expansion of gas generated from the decomposition of the intercalation compounds during the thermal treatment. Microscopically, this process destroys part of the van der Waals interface between adjacent GNPs while maintains the rest. The reserved part makes the exfoliated GNPs be a complete entity, i.e. EG. The size along the *c*-axis (perpendicular to the plane of the graphite layer) increased by more than 100 times. The length of the EG reaches up to several millimeters, while its diameter keeps nearly unchanged and equals the diameter of the plate-like starting

material, i.e. the graphite intercalation compounds. Furthermore, the EGR obtained by mechanically compressing the porous EG becomes compact again and shows the lamellar structure (Fig. 4c). The compression operation maintains the length of EG, while the thickness is reduced to approximately 6 μm. Interestingly, the whole process can be considered as the reconstruction of GNPs, that is, macroscopically from small-sized graphite flake to millimeter-long EGR as illustrated in Fig. 4d. The interlayer van der Waals bondings between adjacent GNPs maintain the morphology of the resulting EGR. The EGR is three orders of magnitude longer and two orders of magnitude wider than the constitutive GNPs (Fig. S2). In consideration of the fabrication process and structural features of the EGR, it can be seen as a new graphite derivative.

The XPS result shows that the element composition of EG includes about 98.7% C content and 1.2% O content (Fig. S3a). The XRD pattern shows a sharp C (002) peak at $2\theta = 26.25$ (the interlayer space, d ~ 0.335 nm) yet no amorphous peak, indicating the graphite lattices are perfect with few defects (Fig. S3b). Besides, the Raman spectrum presents the typical D band (appeared around 1350 cm^{-1}) and G band (appeared around 1580 cm^{-1}) for carbon material (Fig. S3c). The D band represents the disordered carbon, whereas the G band corresponds to the characteristic signal for graphite-like morphology for carbon material [34]. The I_D/I_G intensity ratio for EG is 0.04, indicating the high graphitization degree. Besides, N_2 adsorption measurements (Fig. S4) demonstrated that EG has a large specific surface area of 61.9 $m^2 g^{-1}$ while the EGR has a very low specific surface area of 2.06 $m^2 g^{-1}$. The N_2 adsorption isotherms of EG exhibit unrestricted adsorption at high P/P_0, showing typical features of plate-like particles with slit-shaped pores [46].

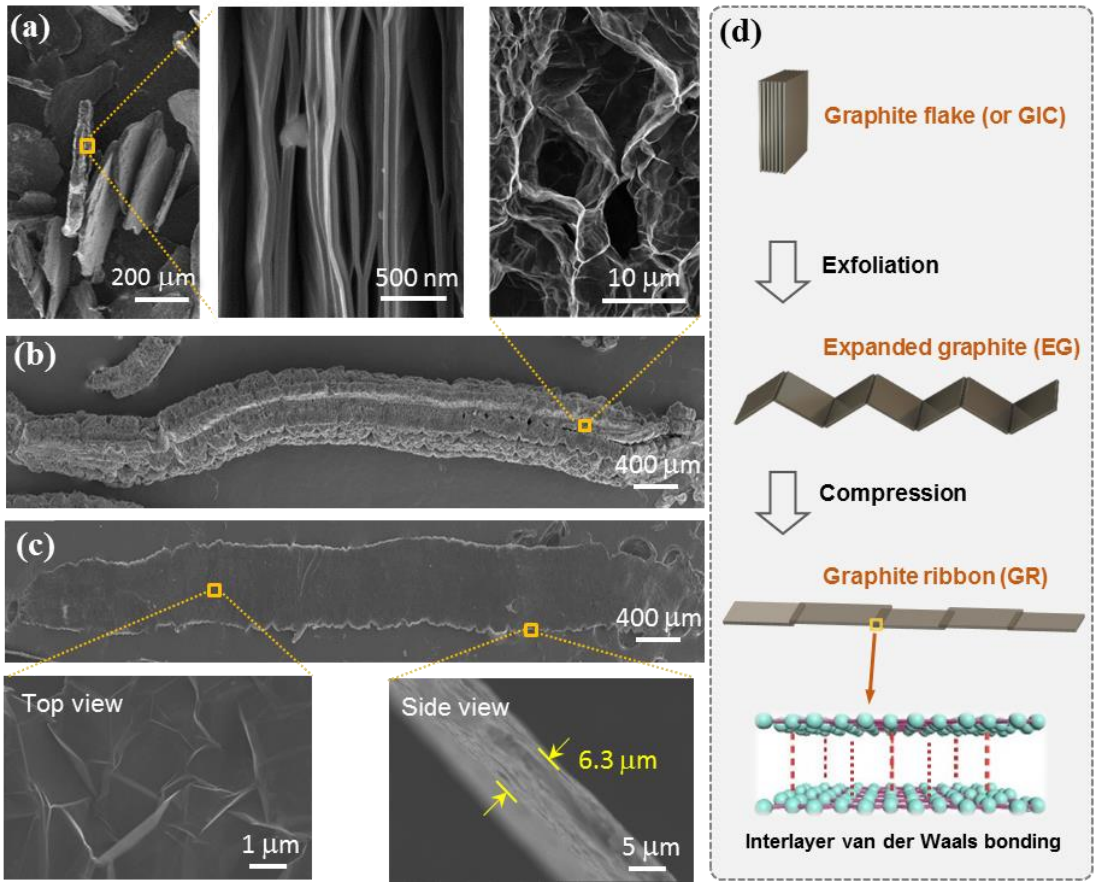

Fig. 4. Morphology of (a) graphite intercalation compounds (GICs), (b) EG, and (c) EGR. (d) The illustration schematic of reconstruction of graphite nanoplatelets.

3.2. Thermal conductivity measurement

Before attaching the sample, the Pt wire was calibrated to obtain the temperature-resistance coefficient and the heat transfer coefficient of the Pt wire in the temperature range from 300K to 380K. The relationship between the heating power and electric resistance of neat Pt wire is shown in Fig. S5. According to Equations (1) and (2) and the intrinsic thermal conductivity of Pt wire (71.6 W m^{-1} K^{-1} [45]) , the heat transfer coefficient of Pt wire was calculated to be about 1.81 W m^{-2} K^{-1} at 300K. Compared with the bare Pt wire, the measured electrical resistance change (ΔR) become smaller at a certain heating power (UI) after the EGR was attached to the Pt wire as shown in Fig. 5. We measured the change of electrical resistance as a function of the Joule heating power. From the slopes of the ΔR - UI curves in Fig. 5 and the temperature-resistance coefficients of Pt hot wire, the apparent thermal resistance of the EGR was calculated

using Equations (2) and (7) to be 8928.9 ± 411.6 K W^{-1}, 6934.8 ± 319.7 K W^{-1}, 4741.0 ± 218.6 K W^{-1}, and 3849.1 ± 177.4 K W^{-1} for the four sample lengths of 7.8 mm, 5.3 mm, 3.4 mm, and 2.0 mm at 300K, respectively (Fig. 6). Here, the uncertainty of the apparent thermal resistance is estimated by:

$$\delta\chi = \sqrt{\left[\frac{\partial\chi}{\partial l_h}\delta l_h\right]^2 + \left[\frac{\partial\chi}{\partial S_h}\delta S_h\right]^2 + \left[\frac{\partial\chi}{\partial h}\delta h\right]^2 + \left[\frac{\partial\chi}{\partial k_s}\delta k_s\right]^2} \quad (9)$$

By nonlinearly fitting the four data points in Fig. 6a into Equation (8) with assuming the emissivity of the EGR to be 1 (ε_s =1), we obtained the thermal conductivity of the EGR sample as 335.6±27.4 W m^{-1} K^{-1} and the TCR at the Pt-sample junction as 1570±373 K W^{-1} at 300K, where the uncertainty represented the fitting standard deviations. During this calculation process, the effective width of the EGR sample was corrected in view of the uneven width of the EGR sample along the longitudinal direction to improve the measurement accuracy. To further improve the uncertainty of measurement, the thermal resistances among the R_h, R_s, and R_c should match each other. The detailed analysis of thermal resistance matching is given in Supplementary Note S1.

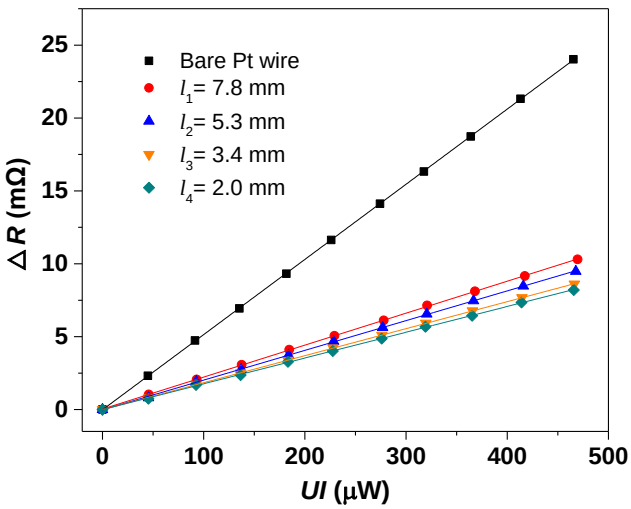

Fig. 5. The changes of electrical resistance as a function of the heating power for bare Pt wire and Pt wire attached with the EGR sample in different effective lengths at 300K.

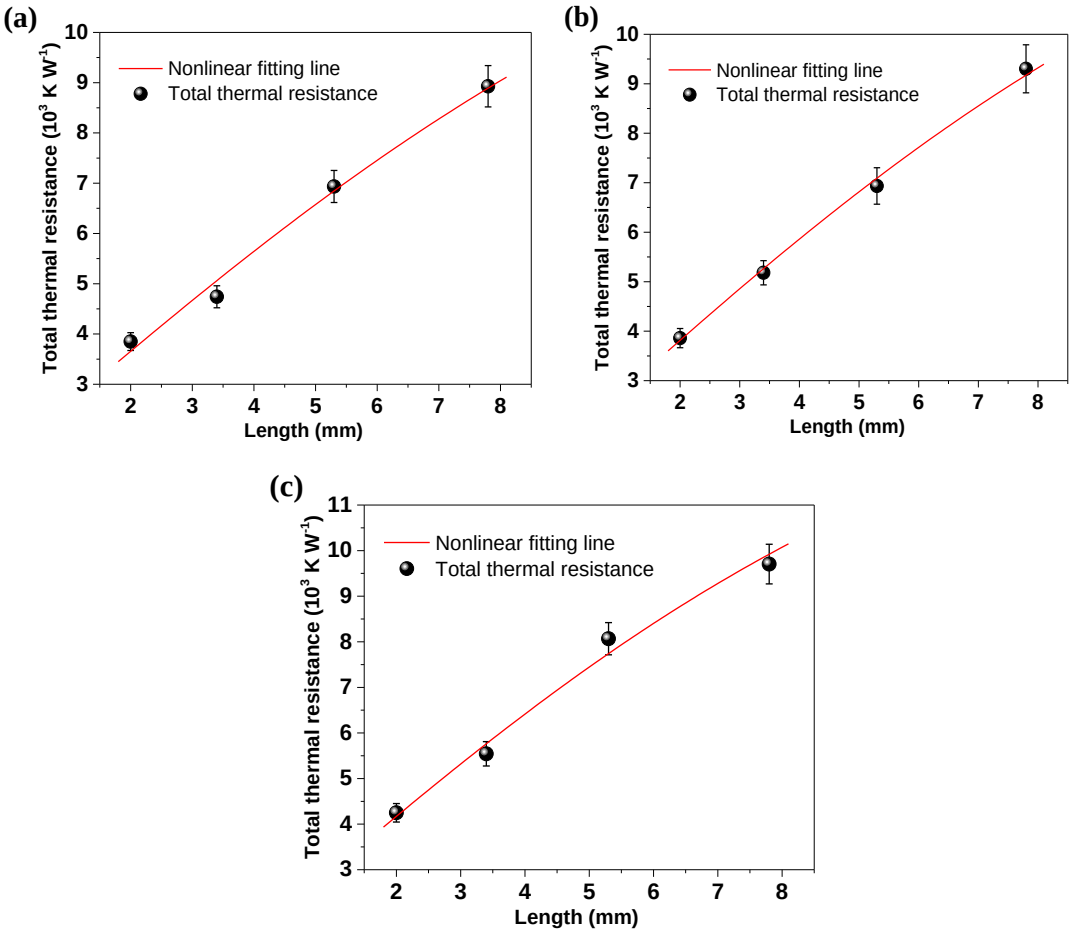

Fig. 6. The measured apparent thermal resistance of EGR as a function of effective sample length at (a) 300 K, (b) 340 K and (c) 380 K.

For every sample length, other two measurement temperatures of 340K and 380K were set to obtain temperature dependence of two thermal resistances, i.e. the thermal resistance of sample itself and the thermal contact resistance. The total thermal resistances as the function of sample length at 340K and 380K are demonstrated in Fig. 6b and c. By calculation, it is found that the both thermal conductivity of the EGR sample and TCR show the temperature dependence. With temperature rising from 300K to 380K, the former decreases from 335.6 ± 27.4 W m^{-1} K^{-1} to 254.8 ±20.8 W m^{-1} K^{-1} (Fig. 7), and the latter increases only a little from 1570 ± 373 K W^{-1} to 1780 ± 243 K W^{-1}.

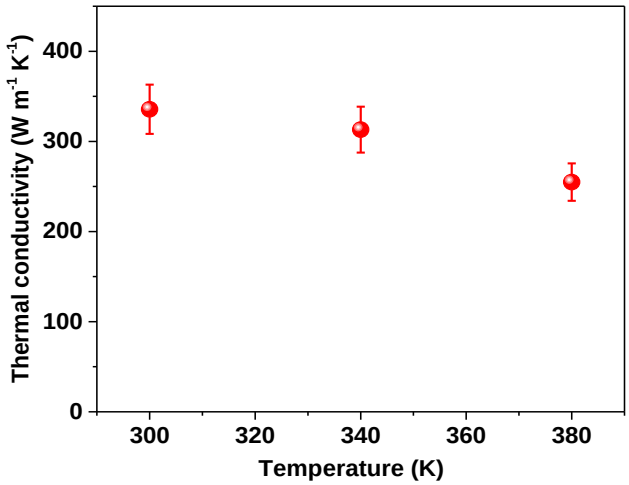

Fig. 7. Temperature dependence of thermal conductivity of the EGR sample from 300 K to 380 K.

3.3. Comparison and potential applications

Fig. 8 compares the thermal conductivities of our measured EGR and other graphite derivations from the literatures. All the thermal conductivities plotted in Fig. 8 are in the lateral or longitudinal direction. The room-temperature thermal conductivity of the EGR is higher than those of macroscopic EG paper, GNP paper, and some graphene papers or films [16,47-49]. Among these graphite products, the EG paper is fabricated by mechanically assembling a large number of EG particles and thus it can be roughly regarded as a stack of EGRs. The high thermal resistance between adjacent EGRs inside the EG paper results in a big difference in the thermal conductivity of EGR and EG paper [16]. The higher the lateral size of the EGR is, the lower the lateral spatial density of high thermal-resistance junction in the as-prepared EG paper is, and the higher the in-plane thermal conductivity of EG paper. The high thermal conductivity of EGR can be attributed to the original van der Waals interactions among its constitutive GNPs. The exfoliation treatment of the graphite flake destroys part of van der Waals interactions but also preserves the rest. The reserved part contributes to lower thermal resistance in the resulting EGR. This is the reason why the EGR has higher thermal conductivity than the GNP paper assembled from highly exfoliated GNP.

The difference in thermal conductivity for the graphene papers or films can be attributed to the discrepancy in the sample preparation method and the uncertainties in

the thermal measurements [48-50]. The room-temperature thermal conductivity of the millimeter-long EGR is much lower than that of suspended monolayer graphene, mainly because the large number of contact interfaces between graphene nanosheets or GNPs inside the EGR introduces intense phonon scattering in thermal transport. Besides, the EGR is ~6 μm thick and the flexural phonon modes are significantly suppressed as compared with monolayer graphene [51-53].

The temperature dependence of thermal conductivity of the EGR agrees well with that of intrinsic graphite [2,54,55]. According to Umklapp's theory, the thermal conductivity of graphene nanosheet firstly increases and then decreases as the temperature rises [52]. For the low-temperature zone, the rise of temperature will cause the increment of quantity of phonon (or spatial density), which contributes to the increment of thermal transport capacity or thermal conductivity. With further temperature rising, the phonon-phonon scattering will become more and more prominent, and weaken the thermal transport capacity. Consequently, the thermal conductivity keeps decreasing. The transition temperature is usually below 300 K. However, for many carbon materials like carbon fiber, graphene paper, and nanostructured graphene, the transition temperature can be larger than 300K [38,39], because other scattering mechanisms like phonon scattering with boundaries, defects and impurities can dominate over Umklapp scattering [56].

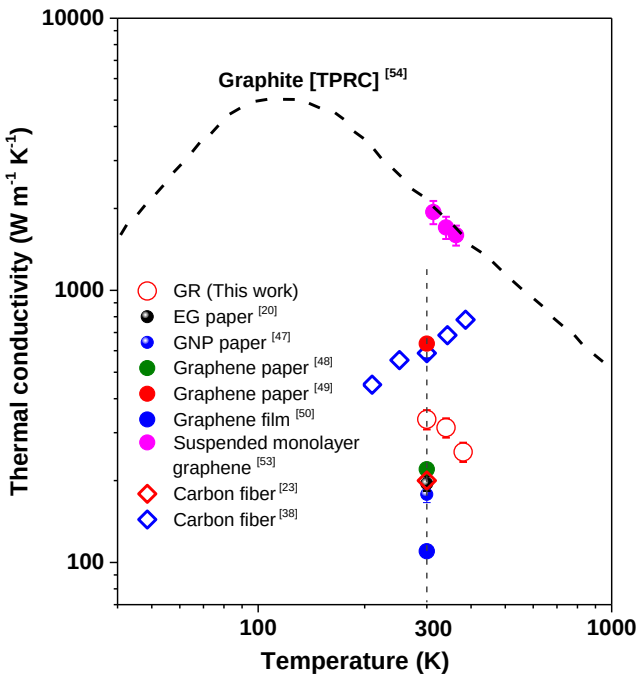

Fig. 8. Comparison of thermal conductivity from different graphite materials and carbon fibers. The test methods for every data are marked in Table S1 in Supplementary Materials. (TPRC: Thermodynamical Properties Research Center at Purdue University, Indiana, USA [54])

Despite the lower thermal conductivity than other high-cost graphite derivatives like carbon nanotubes, graphene, and high-quality carbon fibers, this low-cost EG-based ribbon holds unique advantages in enhancing the thermal conductivity of polymer composites mainly because its precursor, worm-like EG, is porous and can be easily compatible with most organics. The single piece of worm-like EG particle is generally used as a building block to construct the macro-scale bulk graphite block or firstly absorb the liquid organics and then be compressed into a composite block by mechanical compression. Owing to the high pressure, each piece of EG particle can form an EGR inside the as-prepared graphite block or composite block that acts as a millimeter-sized thermally conductive chain. In this case, the connection interface between two adjacent EGRs contributes to the high thermal resistance junction [16], so the spatial density of such high thermal-resistance junction would mainly affect the efficiency in thermal conductivity enhancement. The longer or larger the EGR is, the

lower the spatial density of high thermal-resistance junction is, and the higher the thermal conductivity of the resulting block is. That is the reason that the previously reported composite blocks using nano-microscale graphite or graphene nanosheets as the building block always have the lower thermal conductivity enhancement than those using EG particles as the additives [16]. Based on this consideration, it should also be noted that the long-chain structure of EG should be retained as much as possible during the synthesis of composite block [16]. Besides, the thermal conductivity of the EGR measured in this work provides the indispensable parameter for the mathematic model of thermal conduction in composites, and this would offer an accurate thermal conductivity prediction and help to design highly thermally conductive composites.

4. Conclusions

In this work, we measured the thermal conductivity of an individual millimeter-long expanded graphite ribbon (EGR) using a variable-length T-type method. The EGR is obtained by mechanically compressing one piece of worm-like expanded graphite (EG) particle. During the thermal measurements, the effective length of the sample was successively shortened while maintaining the contact condition between the sample and the probe. By fitting the apparent thermal resistance for four sample lengths into the heat transfer model, we simultaneously obtained the thermal conductivity of the sample and the thermal contact resistance at the junction. The longitudinal thermal conductivity of the EGR reaches up to 335.6±27.4 W m^{-1} K^{-1} at room temperature and decreases to 254.8±20.8 W m^{-1} K^{-1} with the temperature rising from 300K to 380K, much higher than most graphene paper samples and some carbon fibers. This work contributes to the rational thermal design of EG-based composites and provides a valuable reference on how to accurately measure the thermal conductivity of small-sized ribbon- or fiber-like materials.

CRediT authorship contribution statement

Si Wu: Methodology, Investigation, Writing original draft. **Qin-Yi Li:** Methodology, Validation, Writing - review & editing. **Ikuta Tatsuya:** Investigation, Writing - review

& editing. **Kazuhiko Morishita:** Investigation, Writing – review & editing. **Koji Takahashi:** Supervision, Writing – review & editing. **Ruzhu Wang:** Supervision, Writing – review & editing. **Tingxian Li:** Supervision, Writing – review & editing.

Declaration of competing interest

The authors declare that they have no known competing financial interests or personal relationships that could have appeared to influence the work reported in this paper.

Acknowledgments

We thank the National Natural Science Foundation of China under the contract No.51876117 and the National Key R&D Program of China under the contract No.2018YFE0100300. This work was partially supported by JSPS KAKENHI (Grant No. JP20H02090) and JST CREST Grant No. JPMJCR18I1, Japan.

References

[1] H. Song, J. Liu, B. Liu, J. Wu, H. Cheng, F. Kang, Two-Dimensional materials for thermal management applications, Joule 2 (3) (2018) 442-463.

[2] A.A. Balandin, Thermal properties of graphene and nanostructured carbon materials, Nat. Mater. 10 (8) (2011) 569-581.

[3] A.M. Marconnet, M.A. Panzer, K.E. Goodson, Thermal conduction phenomena in carbon nanotubes and related nanostructured materials, Rev. Mod. Phys. 85 (3) (2013) 1295-1326.

[4] K. Pielichowska, K. Pielichowski, Phase change materials for thermal energy storage, Prog. Mater. Sci. 65 (2014) 67-123.

[5] Q. Li, K. Takahashi, X. Zhang, Frequency-domain Raman method to measure thermal diffusivity of one-dimensional microfibers and nanowires, Int. J. Heat Mass Tran. 134 (2019) 539-546.

[6] A. Celzard, J. Mareche, G. Furdin, Modelling of exfoliated graphite, Prog. Mater. Sci. 50 (1) (2005) 93-179.

[7] D.D.L. Chung, A review of exfoliated graphite, J. Mater. Sci. 51 (1) (2016) 554-568.

[8] M. Buzaglo, I.P. Bar, M. Varenik, L. Shunak, S. Pevzner, O. Regev, Graphite-to-graphene: Total conversion, Adv. Mater. 29 (8) (2017) 1603528.

[9] Z. Zhang, G. Alva, M. Gu, G. Fang, Experimental investigation on n–octadecane/polystyrene/expanded graphite composites as form–stable thermal energy storage materials, Energy 157 (2018) 625-632.

[10] S. Wu, T. Li, M. Wu, J. Xu, Y. Hu, J. Chao, et al., Highly thermally conductive and flexible phase change composites enabled by polymer/graphite nanoplatelet-based dual networks for efficient thermal management, Journal of Materials Chemistry A 8 (2020) 20011-20020.

[11] X. Huang, G. Alva, L. Liu, G. Fang, Preparation, characterization and thermal properties of fatty acid eutectics/bentonite/expanded graphite composites as novel form–stable thermal energy storage materials, Sol. Energ. Mat. Sol. C. 166 (2017) 157-166.

[12] N. Zhang, Y. Yuan, X. Wang, X. Cao, X. Yang, S. Hu, Preparation and characterization of lauric–myristic–palmitic acid ternary eutectic mixtures/expanded graphite composite phase change material for thermal energy storage, Chem. Eng. J. 231 (2013) 214-219.

[13] L.W. Wang, S.J. Metcalf, R.E. Critoph, R. Thorpe, Z. Tamainot-Telto, Thermal conductivity and permeability of consolidated expanded natural graphite treated with sulphuric acid, Carbon 49 (14) (2011) 4812-4819.

[14] A. Mallow, O. Abdelaziz, S. Graham, Thermal charging study of compressed expanded natural graphite/phase change material composites, Carbon 109 (2016) 495-504.

[15] S. Wu, T.X. Li, T. Yan, Y.J. Dai, R.Z. Wang, High performance form-stable expanded graphite/stearic acid composite phase change material for modular thermal energy storage, Int. J. Heat Mass Tran. 102 (2016) 733-744.

[16] S. Wu, T. Li, Z. Tong, J. Chao, T. Zhai, J. Xu, et al., Wang, High-performance thermally conductive phase change composites by large-size oriented graphite

sheets for scalable thermal energy harvesting, Adv. Mater. 31 (2019) 1905099.

[17] D.L. Nika, A.A. Balandin, Phonons and thermal transport in graphene and graphene-based materials, Rep. Prog. Phys. 80 (3) (2017) 36502.

[18] J. Kim, D. Seo, H. Park, H. Kim, H. Choi, W. Kim, Extension of the T-bridge method for measuring the thermal conductivity of two-dimensional materials, Rev. Sci. Instrum. 88 (5) (2017) 54902.

[19] X. Xu, L.F. Pereira, Y. Wang, J. Wu, K. Zhang, X. Zhao, et al., Length-dependent thermal conductivity in suspended single-layer graphene, Nat. Commun. 5 (2014) 3689.

[20] J.H. Seol, I. Jo, A.L. Moore, L. Lindsay, Z.H. Aitken, M.T. Pettes, et al., Two-Dimensional phonon transport in supported graphene, Science 328 (2010) 213-216.

[21] L. Qiu, H. Zou, X. Wang, Y. Feng, X. Zhang, J. Zhao, X. Zhang, Q. Li, Enhancing the interfacial interaction of carbon nanotubes fibers by Au nanoparticles with improved performance of the electrical and thermal conductivity, Carbon 141 (2019) 497-505.

[22] L. Qiu, P. Guo, Q. Kong, C.W. Tan, K. Liang, J. Wei, J.N. Tey, Y. Feng, X. Zhang, B.K. Tay, Coating-boosted interfacial thermal transport for carbon nanotube array nano-thermal interface materials, Carbon 145 (2019) 725-733.

[23] Q. Li, K. Katakami, T. Ikuta, M. Kohno, X. Zhang, K. Takahashi, Measurement of thermal contact resistance between individual carbon fibers using a laser-flash Raman mapping method, Carbon 141 (2019) 92-98.

[24] N. C. Gallego, D. D. Edie, B. Nysten, J-P. Issi, J. W. Treleaven, G. V. Deshpande, The thermal conductivity of ribbon-shaped carbon fibers, Carbon 38 (2000) 1003-10.

[25] J. Jumel, F. Lepoutre, J. P. Roger, G. Neuer, M. Cataldi, F. Enguehart, Microscopic thermal characterization of composites, Rev. Sci. Instrum. 74 (2003) 537-9.

[26] Q. Li, K. Xia, J. Zhang, Y. Zhang, Q. Li, K. Takahashi, et al., Measurement of specific heat and thermal conductivity of supported and suspended graphene by a comprehensive Raman optothermal method, Nanoscale 9 (30) (2017) 10784-10793.

[27] Q. Li, W. Ma, X. Zhang, Laser flash Raman spectroscopy method for

characterizing thermal diffusivity of supported 2D nanomaterials, Int. J. Heat Mass Tran. 95 (2016) 956-963.

[28] Q. Li, X. Zhang, Y. Hu, Laser flash Raman spectroscopy method for thermophysical characterization of 2D nanomaterials, Thermochim. Acta 592 (2014) 67-72.

[29] Q. Li, X. Zhang, K. Takahashi, Variable-spot-size laser-flash Raman method to measure in-plane and interfacial thermal properties of 2D van der Waals heterostructures. International Journal of Heat and Mass Transfer 125 (2018)1230-1239.

[30] L. Qiu, N. Zhu, Y. Feng, E.E. Michaelides, G. Żyła, D. Jing, X. Zhang, P.M. Norris, C.N. Markides, O. Mahian, A review of recent advances in thermophysical properties at the nanoscale: From solid state to colloids, Physics Reports 843 (2020) 1-81.

[31] X. Zhang, S. Fujiwara, M. Fujii, Measurements of thermal conductivity and electrical conductivity of a single carbon fiber, Int. J. Thermophys. 21 (2000) 965-80.

[32] M. Fujii, X. Zhang, H. Xie, H. Ago, K. Takahashi, T. Ikuta, et al., Measuring the thermal conductivity of a single carbon nanotube, Phys. Rev. Lett. 95 (2005) 065502.

[33] T. Miao, S. Shi, S. Yan, W. Ma, X. Zhang, K. Takahashi, et al., Integrative characterization of the thermoelectric performance of an individual multiwalled carbon nanotube, J. Appl. Phys. 120 (12) (2016) 124302.

[34] H. Wang, K. Kurata, T. Fukunaga, H. Takamatsu, X. Zhang, T. Ikuta, et al., In-situ measurement of the heat transport in defect- engineered free-standing single-layer graphene, Sci. Rep.-UK 6 (1) (2016) 21823.

[35] J.L. Wang, M. Gu, X. Zhang, Y. Song, Thermal conductivity measurement of an individual fibre using a T type probe method, Journal of Physics D: Applied Physics 42 (10) (2009) 105502.

[36] W. Jang, W. Bao, L. Jing, C.N. Lau, C. Dames, Thermal conductivity of suspended few-layer graphene by a modified T-bridge method, Appl. Phys. Lett.

103 (13) (2013) 133102.

[37] M. Narasaki, Q. Li, T. Ikuta, J. Miyawaki, K. Takahashi, Modification of thermal transport in an individual carbon nanofiber by focused ion beam irradiation, Carbon 153 (2019) 539-544.

[38] J. L. Wang, M. Gu, W. G. Ma, X. Zhang, Y. Song, Temperature dependence of the thermal conductivity of individual pitch-derived carbon fibers, New Carbon Mater. 23 (2008) 259-63.

[39] Q. Li, K. Takahashi, H. Ago, X. Zhang, T. Ikuta, T. Nishiyama, et al., Temperature dependent thermal conductivity of a suspended submicron graphene ribbon, J. Appl. Phys. 117 (6) (2015) 65102.

[40] Q. Li, K. Takahashi, X. Zhang, Comment on "Divergent and Ultrahigh Thermal Conductivity in Millimeter-Long Nanotubes", Physical Review Letters 119 (17) (2017) 179601.

[41] Q. Li, J. Liu, H. Wang, X. Zhang, K. Takahashi, Optical absorptance measurement of an individual multiwall carbon nanotube using a T type thermal probe method, Rev. Sci. Instrum. 84 (10) (2013) 104905.

[42] Q. Li, X. Zhang, T-type Raman spectroscopy method for determining laser absorption, thermal conductivity and air heat transfer coefficient of micro/nano fibers, Thermochim. Acta 581 (2014) 26-31.

[43] Q. Li, T. Feng, W. Okita, Y. Komori, H. Suzuki, T. Kato, et al., Enhanced thermoelectric performance of As-Grown suspended graphene nanoribbons, ACS Nano 13 (8) (2019) 9182-9189.

[44] J. Huang, A. Fan, X. Xia, S. Li, X. Zhang, *In situ* thermal conductivity measurement of single-crystal zeolitic imidazolate framework-8 by Raman-Resistance temperature detectors method, ACS Nano 14(10) (2020) 14100–14107.

[45] F. P. Incropera, D. P. DeWitt, Fundamentals of Heat and Mass Transfer (New York: Wiley) (2002) 907.

[46] T. Zhao, S. She, X. Ji, X. Guo, W. Jin, R. Zhu, et al., Expanded graphite embedded with aluminum nanoparticles as superior thermal conductivity anodes for high-performance lithium-ion batteries, Sci. Rep.-UK 6 (1) (2016) 33833.

[47] J. Xiang, L.T. Drzal, Thermal conductivity of exfoliated graphite nanoplatelet paper, Carbon 49 (3) (2011) 773-778.

[48] Z.L. Hou, W.L. Song, P. Wang, M.J. Meziani, C.Y. Kong, A. Anderson, et al., Flexible graphene-graphene composites of superior thermal and electrical transport properties, ACS Appl. Mater. Inter. 6 (2014) 15026–15032.

[49] J. Gao, C. Meng, D. Xie, C. Liu, H. Bao, B. Yang, et al., Temperature dependent thermal transport in graphene paper above room temperature, Appl. Therm. Eng. 150 (2019) 1252-1259.

[50] Y. Zhang, M. Edwards, M.K. Samani, N. Logothetis, L. Ye, Y. Fu, et al., Characterization and simulation of liquid phase exfoliated graphene-based films for heat spreading applications, Carbon 106 (2016) 195-201.

[51] D.L. Nika, A.A. Balandin, Phonons and thermal transport in graphene and graphene-based materials, Rep. Prog. Phys. 80 (3) (2017) 36502.

[52] Q. Y. Li, Q. Hao, T. H. Zhu, M. Zebarjadi, K. Takahashi, Nanostructured and Heterostructured 2D Materials for Thermoelectrics. Engineered Science 2020, DOI: 10.30919/es8d1136

[53] X. K. Gu, & R. G. Yang, Phonon transport and thermal conductivity in two-dimensional materials. Ann. Review. Heat Tran. 19 (2016) 1-65.

[54] Y. S. Touloukian, Thermophysical Properties of Matter (IFI/Plenum, New York, 1970–1979).

[55] H. Wang, K. Kurata, T. Fukunaga, X. Zhang, H. Takamatsu, Width dependent intrinsic thermal conductivity of suspended monolayer graphene, Int. J. Heat Mass Tran. 105 (2017) 76-80.

[56] G. Fugallo, A. Cepellotti, L. Paulatto, M. Lazzeri, N. Marzari, F. Mauri, Thermal conductivity of graphene and graphite: Collective excitations and mean free paths, Nano Lett. 14 (11) (2014) 6109-6114.